Journal of Inorganic and Organometallic Polymers and Materials
https://doi.org/10.1007/s10904-021-02032-y

Facile Synthesis of CuO and Ag Nanoparticles by Thermal Decomposition of Novel Schiff Base Complexes

Mamdouh M. Abdelghany[1] · **Ibrahim S. Ahmed**[1] · **Hassan A. Dessouki**[1] · **Ehab A. Abdelrahman**[1]

Received: 8 April 2021 / Accepted: 17 May 2021

Abstract

In this paper, a new Schiff base was synthesized via the condensation reaction between 3-methyl-4-amino-5-mercapto-1,2,4 triazole and 2-hydroxy-1-naphthaldehyde. Also, the Cu(II) and Ag(I) complexes were synthesized. Besides, the CuO and Ag nanoparticles were synthesized via thermal decomposition of Cu(II) and Ag(I) complexes at 800 °C. The products were characterized using various techniques such as FT-IR, ^{1}HNMR, elemental microanalysis, UV–Vis spectrophotometer, mass spectrophotometry, magnetic susceptibility measurements, molar conductance measurements, ESR, thermal analysis (TGA and DSC), XRD, FE-SEM, and HR-TEM. The average crystallite size of CuO and Ag nanoparticles is 55.61 and 52.07 nm, respectively. The direct band gap of the CuO and Ag samples is 2.95 and 3.20 eV, respectively. The synthesized nanoparticles were utilized as photocatalysts for the degradation of methylene blue dye in aqueous media. The % degradation of methylene blue dye (MB) is 94.25% within 20 min and 90.42% within 210 min in case of utilizing ($CuO + H_2O_2 + UV$) and ($Ag + H_2O_2 + UV$), respectively. The products were tested for studying their antimicrobial activities against some bacterial and fungal strains. The synthesized complexes and their nanoparticles show moderate activity against *Escherichia coli* and *Staphylococcus aureus* bacterial strains. All the products showed no activity against *Aspergillus flavus* and *Candida albicans* fungal strains. Also, the synthesized compounds were screened for studying their cytotoxic activity against the human breast cancer cell line (MCF-7). The results revealed that the Cu(II) complex could be nominated as a potential anticancer agent because it showed a cytotoxic activity ($IC_{50} = 7.33 \pm 0.6$ µg/mL) nearly equal to that of cisplatin drug ($IC_{50} = 5.71$ µg/mL).

Keywords Schiff base complexes · Thermal decomposition · CuO and ag nanoparticles · Photocatalytic degradation · Antimicrobial · Anticancer

1 Introduction

Schiff base compounds and their transition metal complexes exhibit major importance for their biological properties, encompass antibacterial, antifungal, and anticancer properties [1–5]. The complexes based on (2-((1H-Benzo [d] imidazole-4ylimmino) methyl phenol) with Cu(II), Co(II), and Zn(II) ions showed higher inhibition zone in microbial activities against various micro-organisms such as *Candida albicans*, *Staphylococcus aureus*, *Pseudomonas aeruginosa*, and *Escherichia coli*. Furthermore, the highest binding affinity to DNA value was in the copper complex as reported by Kalarani et. al. [6]. Shiju et. al., reported that the resultant complex of the combination of 4-nitrobenzaldehyde-glycylglycine and metal ions such as Co(II), Zn(II), and Cu(II) have promising inhibition for Human Cervical Cancer Cells (HeLa) and Colon Cancer Cells (HCT116) [7]. Notably, Schiff base compounds accommodate bioactive triazole moiety and its derivatives possess prominent value as antimicrobial and anticancer agents [8, 9]. Amer et. al., synthesized Cu(II) complexes via the combination of copper with ligand derived from triazole and purine derivatives. The synthesized complexes have moderate activity with IC_{50} of 8.7, 9.8, and 10.3 against liver carcinoma (HEPG2), colon carcinoma (HCT116), and breast cancer (MCF7) cell lines, respectively [10]. Singh et. al., synthesized Zn(II) complexes from Schiff base compounds based on 1,2,4 triazole derivative precisely 3-substituted phenyl-4-amino-5-hydrazino-1, 2, 4-triazole. The synthesized Schiff bases and their Zn(II) complexes were tested for their antibacterial activities against *E. coli* and bacillus subtilis. Also, they tested for their antifungal

---

✉ Ehab A. Abdelrahman
dr.ehabsaleh@yahoo.com; ehab.abdelrahman@fsc.bu.edu.eg

[1] Chemistry Department, Faculty of Science, Benha University, Benha 13518, Egypt

activities against carvularia pallescence, colletotrichum falcatum, fusarium oxysporium, and aspergillus niger. Additionally, the results confirmed that the synthesized Schiff bases show moderate antimicrobial activities whereas the Zn(II) complexes show high antimicrobial activities [11]. Recently, transition metal complexes have been exploited as precursors by Nassar et. al. in the preparation of many nanomaterials such as Co_3O_4, CuO, and NiO through thermal decomposition [12–14]. This method is characterized by the production of nanomaterials with small crystallite sizes and various morphologies. Particularly, nanomaterials occupy their great importance in water treatment by using them in the adsorption and photocatalytic degradation techniques [15, 16]. One of the main advantages of the photocatalytic degradation technique is that it is using nanomaterials as a catalyst in presence of sunlight or UV irradiation to produce free radicals which can decompose numerous organic pollutants such as dyes [17, 18]. Ahmed et. al., prepared CuO nanoparticles using the thermal treatment of the pre-synthesized Cu(II) flubendazole complex. The produced CuO nanoparticles showed high efficiency when used as a photocatalyst for the degradation of the methylene blue (MB) dye under UV irradiation [19]. Muthuvel et. al., showed the great potential of the CuO nanoparticles as a photocatalyst with a degradation efficiency of the MB dye up to 97% under sunlight irradiation. Also, they utilized the nanoparticles as an antibacterial agent against bacillus subtilis, staphylococcus saprohyticus, *E. coli*, and *Pseudomonas aeruginosa* [20]. Thermal decomposition of complexes is considered one of the simplest methods for producing nanomaterials with small crystallite sizes and various morphologies. In this paper, a novel Schiff base was facilely synthesized via the condensation of 3-methyl-4-amino-5-mercapto-1,2,4-triazole with 2-hydroxy-1-naphthaldehyde. Then, Cu(II) and Ag(I) complexes were facilely synthesized via the condensation of Schiff base with $CuCl_2.2H_2O$ and $AgNO_3$, respectively. Besides, CuO and Ag nanoparticles were facilely synthesized via thermal decomposition of the synthesized complexes. The synthesized nanoparticles were utilized as a photocatalyst for the efficient degradation of methylene blue dye in the presence of H_2O_2. Also, the biological and antitumor activities of the products against human breast cancer cell line (MCF-7) were studied.

2 Experimental

2.1 Chemicals

The used chemicals are hydrazine hydrate (H_6N_2O), carbon disulfide (CS_2), glacial acetic acid ($C_2H_4O_2$), 2-hydroxy-1-naphthaldehyde ($C_{11}H_8O_2$), ethanol (C_2H_6O), N,N-dimethylformamide (C_3H_7NO), sulfuric acid (H_2SO_4), copper(II) chloride dihydrate ($CuCl_2{\cdot}2H_2O$), silver(I) nitrate ($AgNO_3$), sodium acetate trihydrate ($C_2H_9NaO_5$), and methylene blue dye ($C_{16}H_{18}ClN_3S$). All the chemicals were supplied from Sigma–Aldrich Company and used without any further purification.

2.2 Synthesis of Schiff Base

Notably, 3-methyl-4-amino-5-mercapto-1,2,4-triazole was synthesized as reported by Aly et. al. [14]. Also, a 40 mL ethanolic solution of 3-methyl-4-amino-5-mercapto-1,2,4 triazole (0.2603 g, 2 mmol) was added to a 20 mL ethanolic solution of 2-hydroxy-1-naphthaldehyde (0.3444 g, 2 mmol) then the mixture was refluxed for 4 h. Besides, few drops of a dehydrating agent (Concentrated H_2SO_4) was added and the reflux was continued for 2 h. The formed yellow precipitate was filtered off after cooling, washed carefully several times with ethanol, and dried in a desiccator over anhydrous $CaCl_2$.

2.3 Synthesis of the Cu(II) and Ag(I) Complexes

The Schiff base solution was prepared by dissolving 0.2843 g of Schiff base (1 mmol) in 10 mL DMF. Also, the Cu(II) solution was prepared by dissolving 0.1705 g of $CuCl_2{\cdot}2H_2O$ (1 mmol) in 20 ethanol. Besides, the Ag(I) solution was prepared by dissolving 0.1699 g of $AgNO_3$ (1 mmol) in 10 ml DMF. Moreover, the Cu(II) or Ag(I) solution was added to the Schiff base solution then the mixture was refluxed for 4 h. After that, 0.2722 g sodium acetate trihydrate (2 mmol) was dissolved in 10 mL ethanol and added to the reaction mixture. Then, the reflux was continued for 4 h. It is worth noting that in the case of the Ag(I) complex the half volume of the solvent was vaporized. After a sufficient period for cooling, the complex (orange for Ag(I) complex or green for Cu(II) complex) was filtered off, washed carefully several times with ethanol, and dried in a desiccator over anhydrous $CaCl_2$.

2.4 Synthesis of CuO and Ag Nanoparticles

The CuO and Ag nanoparticles were synthesized by thermal decomposition of Cu(II) and Ag(I) complexes at 800 °C, respectively.

2.5 Characterization Tools

Perkin Elmer 1650 spectrometer (400–4000 cm^{-1}) was used to record Fourier transform infrared (FT-IR) spectra using KBr disks. Using tetramethylsilane (TMS) as an internal standard ^{1}HNMR spectrum was recorded in DMSO-d_6 on a Bruker 300 MHz spectrometer at room temperature. Elemental microanalysis for C, H, N, O, and S was performed using CHNS-932 (LECO) Vario analyzer. The electronic spectra were recorded by Jasco V-670 UV–Vis spectrophotometer. The mass spectrum was carried out on direct probe controller inlet part to single quadrupole mass analyzer in (Thermo scientific GC MS) model (ISQLT) (mass range 40–1000 dalton) using Thermo X-Calibur software. The measurements of magnetic susceptibility were carried out using Sherwood scientific magnetic balance, Cambridge science. The thermal analysis (TGA and DSC) was performed using a LAB-SYS evo–SETARAM instruments. Klystron-X-band EMX spectrometer was used to record the ESR spectrum. Molar conductivities were measured using Jenco conductivity meter 3173. Phase identification using X-ray diffraction (XRD) was recorded by PAN analytical XRD employing Cu K_α X-ray ($\lambda = 1.5406$ Å). The morphology of the samples was measured by a field emission scanning electron microscope (FE-SEM; JSM-6510LV; JEOL). The microstructure of the samples was recorded by a high-resolution transmission electron microscope (HR-TEM; KEM-2100; JEOL). The melting point of the Schiff base was measured using the Afon DMP 100 melting point device.

2.6 Photocatalytic Degradation of the Methylene Blue Dye

The photocatalytic degradation of the methylene blue dye under UV irradiation source has been studied using CuO and Ag nanoparticles. The photocatalytic procedure was carried out by placing 0.1 g of each catalyst in a Pyrex beaker. Then, 50 mL of 20 mg/L of methylene blue dye solution was added to the weighed catalyst. The mixture was kept in dark and magnetically stirred for 2 h to reach equilibrium. After that, the beaker was exposed to UV irradiation for a specific time. It is worthy to mention that a box contains 4 UV lamps (UV-CG13T8, 15 W) that used for the irradiation. Before measuring the absorption spectra, each fraction was centrifuged to separate the catalyst from the solution. Then, the filtrate was examined to measure the methylene blue dye concentration (at 664 nm) utilizing a preconstructed calibration curve using UV–VIS spectrophotometer. Moreover, 2 mL of 2 M of hydrogen peroxide (H_2O_2) was used in the presence of each catalyst and UV source in the same manner as described above. The % degradation of the methylene blue dye was calculated using Eq. (1) [17].

$$\%\ \text{degradation} = \frac{C_d - C_t}{C_d} 100 \tag{1}$$

where C_d and C_t are the concentration of the MB dye (mg/L) after equilibrium and at time *t*, respectively.

2.7 Biological Activity Studies

The biological activities studies were carried out using the modified Kirby-Bauer disc diffusion method [21]. Briefly, 100 µl of the tested bacteria/fungi were grown in 10 ml of fresh media until they reached a count of approximately 10^8 cells/ml for bacteria or 10^5 cells/ml for fungi [22]. 100 µl of microbial suspension was spread onto agar plates corresponding to the broth in which they were maintained. Isolated colonies of each organism that might be playing a pathogenic role were selected from primary agar plates and tested for susceptibility by disc diffusion method [23]. Plates inoculated with filamentous fungi as *Aspergillus flavus* at 25 °C for 48 h. Gram-positive bacteria as *S. aureus*, and Gram-negative bacteria as *E. coli*, were incubated at 35–37 °C for 24–48 h. Also, yeast as *C. albicans* incubated at 30 °C for 24–48 h. Then, the diameters of the inhibition zones were measured in millimeters. It is worthy to mention that standard discs of Ampicillin (Antibacterial agent), Amphotericin B (Antifungal agent) served as positive controls for antimicrobial activity. Filter discs with a diameter of 8.0 mm impregnated with 10 µl of solvent (DMSO), were used as a negative control. When a filter paper disc impregnated with the tested chemical is placed on agar the chemical will diffuse from the disc into the agar. This diffusion will place the chemical in the agar only around the disc. The solubility of the chemical and its molecular size will determine the size of the area of chemical infiltration around the disc. If an organism is placed on the agar it will not grow in the area around the disc if it is susceptible to the chemical. This area of no growth around the disc is known as the "Zone of inhibition".

2.8 In Vitro Cytotoxic Activity

The cytotoxic activity was evaluated against the human breast cancer cell line (MCF-7) using viability assay [24]**.** The cells were seeded in a 96-well plate at a cell concentration of 1×10^4 cells per well in 100 µl of growth medium. A fresh medium containing different concentrations of the tested samples was added after 24 h of seeding. Serial two-fold dilutions of the tested compounds were added to confluent cell monolayers dispensed into 96-well, flat-bottomed microtiter plates (Falcon, NJ, USA) using a multichannel pipette. The microliter plates were incubated at 37 °C in a humidified incubator with 5% CO_2 for a period of 24 h. Three wells were used for each concentration of the tested sample. Control cells were incubated without a test sample and with or without DMSO. The little percentage of DMSO present in the wells (maximal 0.1%) was found not to affect the experiment. After incubation of the cells at 37 °C, for 24 h, the viable cells yield was determined by a colorimetric method. In brief, after the end of the incubation period, media were aspirated and the crystal violet solution (1%) was added to each well for at least 30 min. The stain was removed and the plates were rinsed using tap water until all excess stain is removed. Glacial acetic acid (30%) was then added to all wells and mixed thoroughly, and then the absorbance of the plates was measured after gently shaken on a Microplate reader (TECAN, Inc.), using a test wavelength of 490 nm. All results were corrected for background absorbance detected in wells without added stain. Treated samples were compared with the cell control in the absence of the tested compounds. All experiments were carried out in triplicate. The cell cytotoxic effect of each tested compound was calculated**.** The optical density was measured with the Microplate reader to determine the number of viable cells then the percentage of viability was calculated using Eq. (2).

$$\text{The percentage of viability } = \frac{\text{ODt}}{\text{ODc}} * 100\% \tag{2}$$

where ODt and ODc is the mean optical density of wells treated with the tested sample and the mean optical density of untreated cells, respectively. The relation between surviving cells and drug concentration is plotted to get the survival curve of each tumor cell line after treatment with the specified compound. The 50% inhibitory concentration (IC_{50}) is the concentration required to cause toxic effects in 50% of intact cells. It was estimated from graphic plots of the dose–response curve for each concentration.

3 Results and Discussion

3.1 Characterization of Schiff Base

3.1.1 ^{1}HNMR

Scheme 1 represents the proposed structure of the synthesized Schiff base. Figure 1A and B represents ^{1}HNMR spectra for the synthesized Schiff base in DMSO-d_6 and D_2O, respectively. The results exhibited signals (δ, ppm): 7.24–8.70 (m, 6H, Ar–H), 2.50 (s, 3H, CH_3-triazole), 10.51 (s, 1H, –CH), 11.31 (s, 1H, NH-triazole), and 13.51 (s, 1H, –SH). The absence of –NH triazole signal in the D_2O spectrum emphasizes the presence of –NH on triazole moiety [12–14].

3.1.2 FT-IR

Figure 2 represents the FT-IR spectrum of the synthesized Schiff base. The characteristic band, that existed at 1605 cm^{-1}, was assigned to the stretching vibration azomethine group (–C=N–). The absence of the sharp stretching vibration of the carbonyl group (–C=O) (at 1700 cm^{-1}) confirms the successful formation of the Schiff base. The bands, which were observed at 2747, 2939, 3140, and 3233 cm^{-1}, are attributed to stretching vibrations of (–SH), (–CH) aliphatic of the methyl group, (–CH) aliphatic of the azomethine group, and (–CH) aromatic, respectively. The observed band at 3418 cm^{-1} is due to stretching vibration of (–NH) and/or (–OH). The multi-bands, that appeared at 1474 and 1535 cm^{-1}, are due to stretching vibrations of (–C=C–) of the aromatic rings. The presence of bands at 1088, 1165, and 1258 cm^{-1} are attributed to stretching vibrations of (–N–N–), (–C–O–), and (–C=S–), respectively. The observed bands at 1335 and 1396 cm^{-1} are due to bending vibrations of (–OH), and (–CH) of the methyl group, respectively. The multi-bands, which were observed in the range from 524 to 964 cm^{-1}, are due to (–CH–) out-of-plane bending vibrations of the aromatic moiety [12–14].

3.1.3 Melting Point, Mass Spectrum, and Elemental Analysis

The melting point of the synthesized Schiff base is 256.8 °C. This sharp melting point confirms the purity of the product.

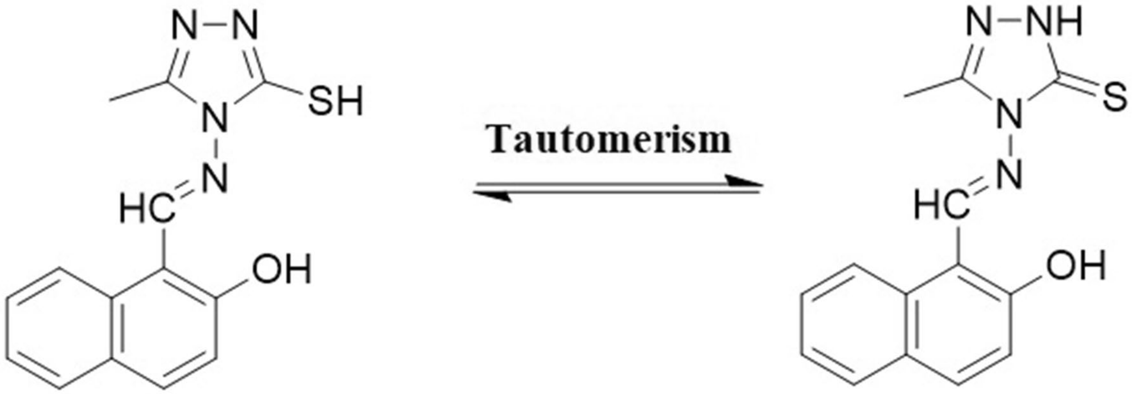

Scheme 1 The proposed structure of the synthesized Schiff base

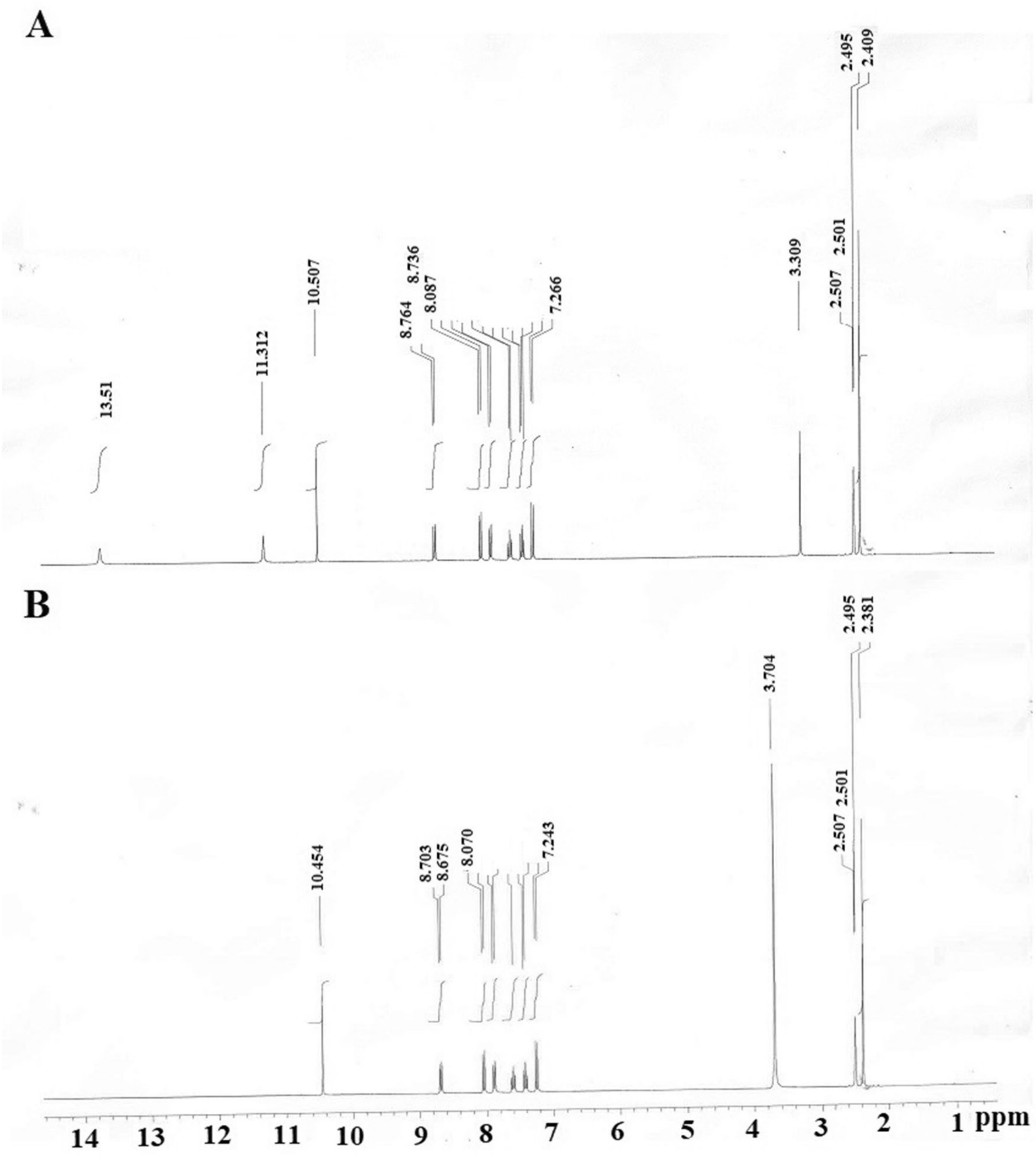

Fig. 1 ^{1}H- NMR spectra for the synthesized Schiff base in DMSO-d$_6$ (**A**) and D$_2$O (**B**)

The calculated molecular weight of the synthesized Schiff base is 284.33 amu and matched well with that calculated from the mass analysis as clarified in Fig. 3. The calculated percent of the elements of the synthesized Schiff base ($C_{14}H_{12}N_4OS$) is 59.14%C, 4.25%H, 19.72%N, 5.63%O, and 11.26%S. The practical percent of the elements of the synthesized Schiff base is 59.26%C, 4.18%H, 19.59%N, 5.94%O, and 11.03%S. Hence, the results obtained from elemental analysis were in good agreement with theoretical values. Thus, this confirms the proposed formula of the synthesized Schiff base as shown in Scheme 1.

3.1.4 Electronic Spectra

Figure 4 represents the UV–Vis spectra for the synthesized Schiff base in different solvents. There are 2 bands (K & β) due to π–π^* transition at (219&283 nm), (219, 281 nm), (218, 280 nm), (208, 281 nm), and (216, 290 nm) in the case of using DMF, EtOH, MeOH, toluene, and chloroform as solvents, respectively as shown in Table 1. Also, there is one band due to n–π^* electronic transition confirmed the presence of the azomethine group (–C=N–) at 322, 324, 321, 324, and 324 nm in the case of using DMF, EtOH, MeOH,

Fig. 2 FT-IR spectrum of the synthesized Schiff base

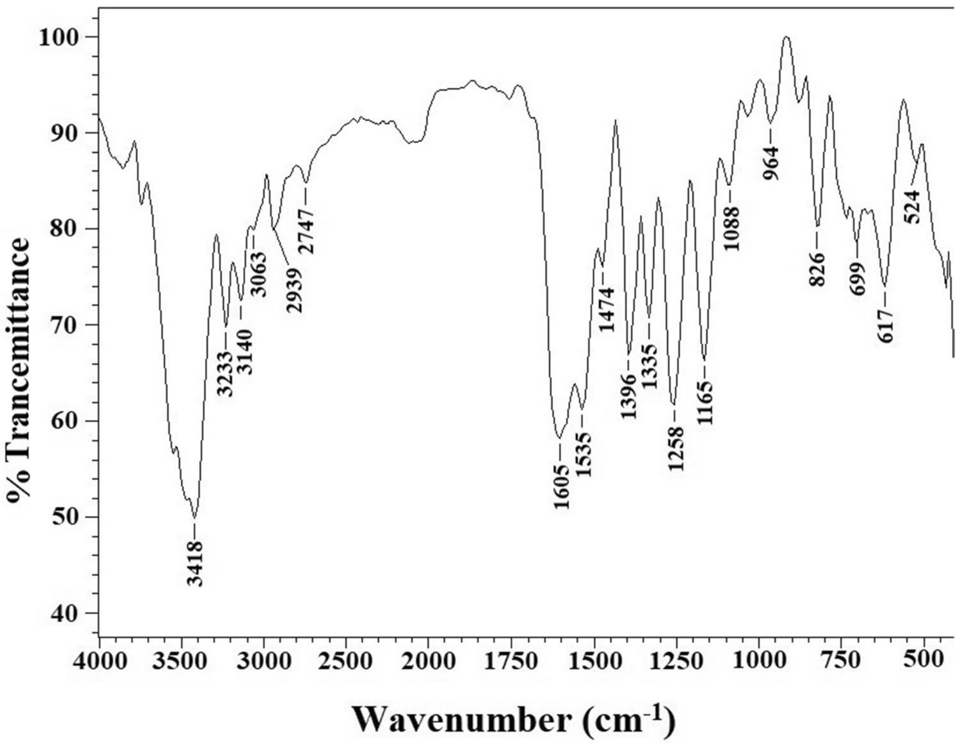

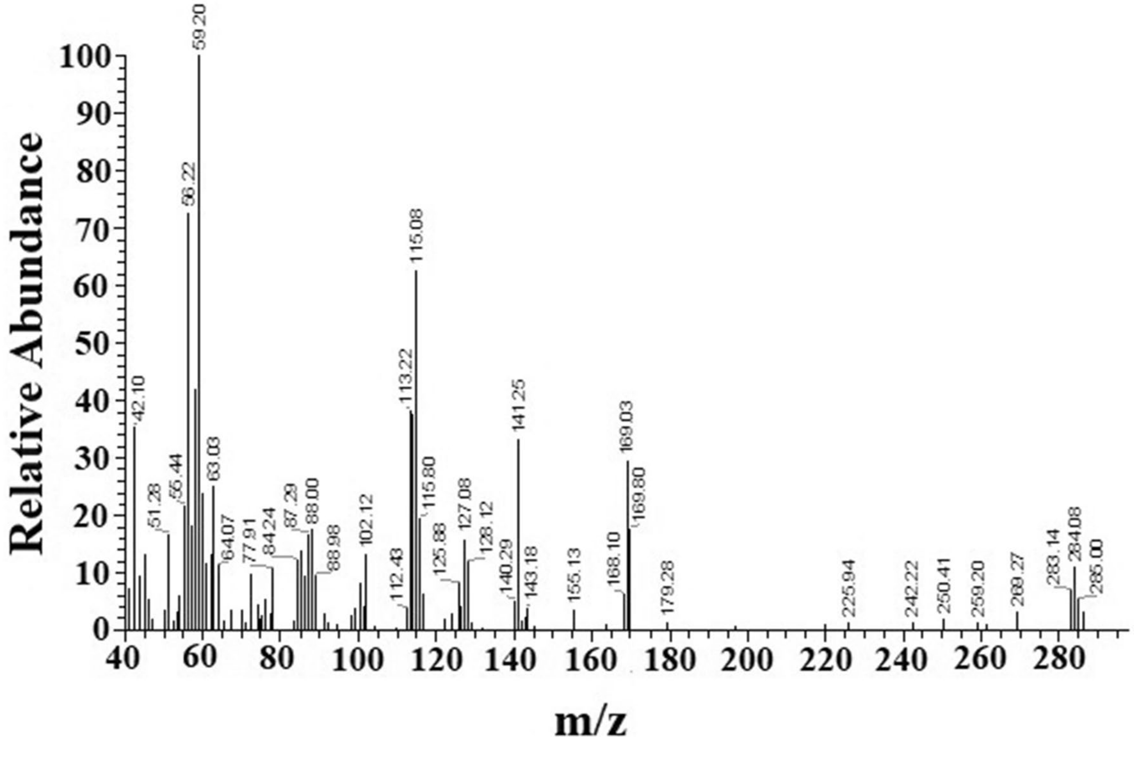

Fig. 3 Mass spectrum of the synthesized Schiff base

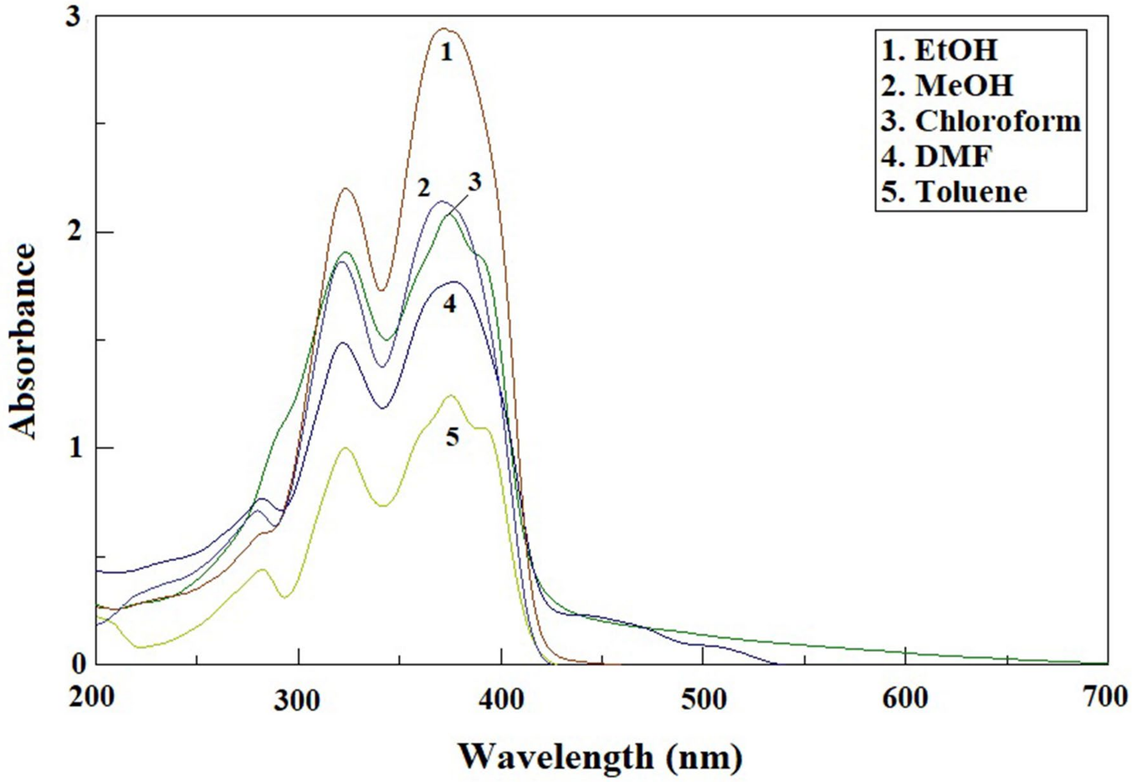

Fig. 4 UV–Vis spectra for the synthesized Schiff base in different solvents

Table 1 The electronic transitions of the synthesized Schiff base in different solvents

Solvent	π–π*		n–π*	Charge transfer
	K band	β band		
DMF	219	283	322	377
EtOH	219	281	324	372
MeOH	218	280	321	370
Tolune	208	281	324	375
Chloroform	216	290	324	375

toluene, and chloroform as solvents, respectively. Additionally, there is one band due to charge transfer on the triazole moiety as presented in scheme 1 at 377, 372, 370, 375, and 375 in the case of using DMF, EtOH, MeOH, toluene, and chloroform as solvents, respectively [12–14].

3.2 Characterization of Ag(I) and Cu(II) Schiff Base Complexes

3.2.1 Molar Conductivity Measurements

The Molar conductivity was measured for Ag(I) and Cu(II) Schiff base complexes at a concentration of 0.01312 M in DMSO at 25 °C, using the following Eq. (3) [12–14].

$$\Lambda_m = \frac{\kappa * 1000}{c} \tag{3}$$

where Λ_m is the molar conductivity, κ is the specific conductance, and c is the molar concentration. The molar conductivity for Ag(I) and Cu(II) complexes is 25 and 28 Ω^{-1} $mol^{-1}cm^2$, respectively. These low conductivity values indicate the non-electrolytic nature of the formed complexes with the absence of Cl^- or NO_3^- anions outside the coordination sphere. Scheme 2 represents the proposed structure of Ag(I) and Cu(II) complexes.

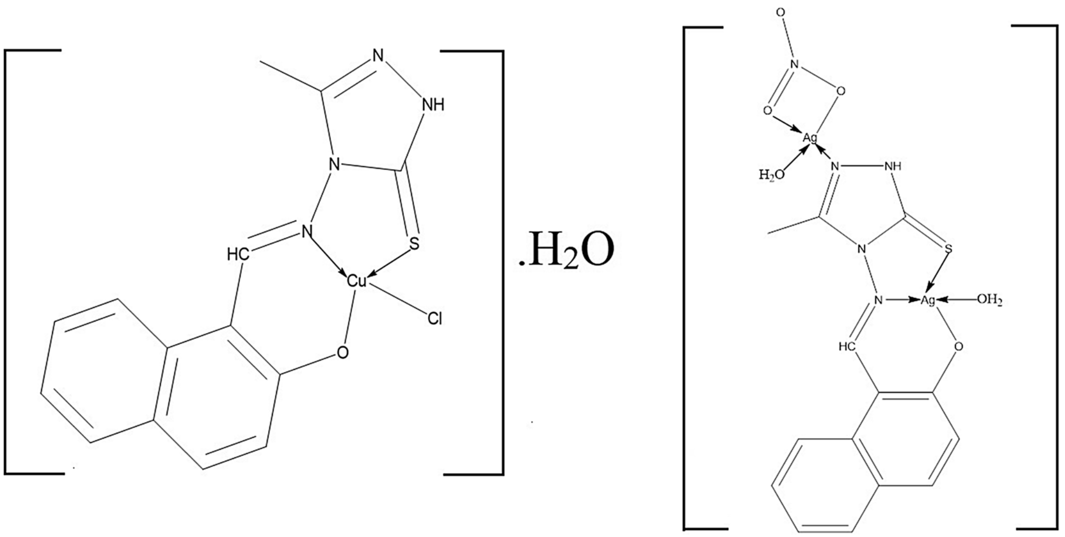

Scheme 2 The proposed structure of the synthesized Ag(I) and Cu(II) complexes

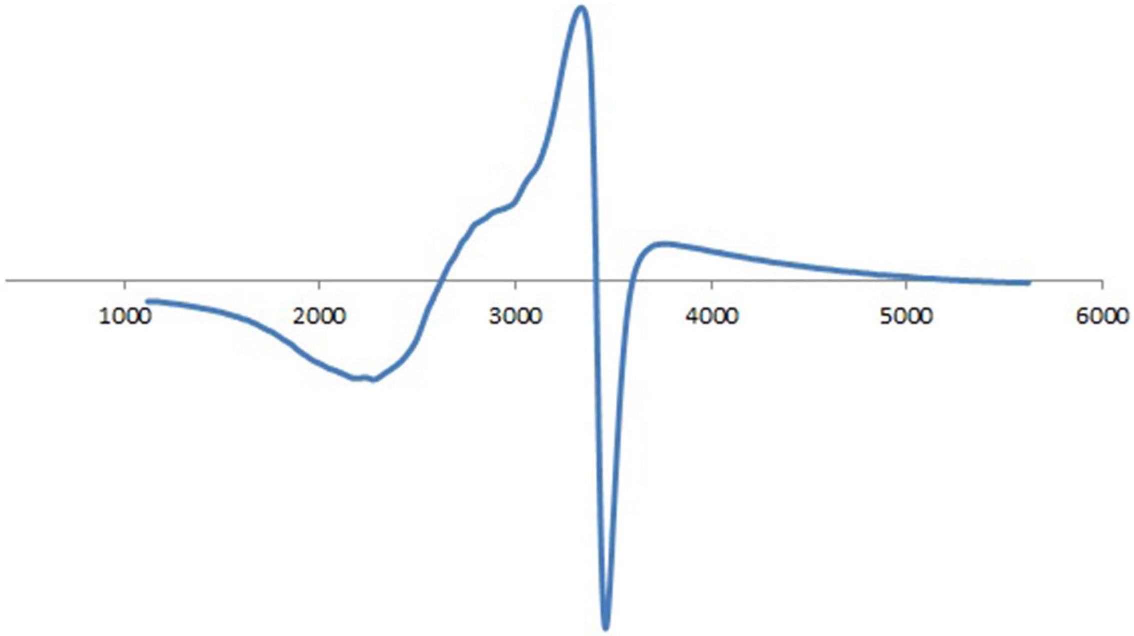

Fig. 5 ESR of the synthesized Cu(II) complex

3.2.2 ESR and Magnetic Susceptibility Studies for Cu (II) Complex

The ground state electronic distribution of Cu(II) is $t_{2g}^{6}\, e_{g}^{3}$ which yields $^{2}E_{g}$ term. The excited electronic state is $t_{2g}^{5}\, e_{g}^{4}$ which yields $^{2}T_{2g}$ term. The possible transition in the case of the octahedral crystal field is $^{2}E_{g} \rightarrow {}^{2}T_{2g}$. Because of the Jahn–Teller effect, $^{2}E_{g}$ state splits into $^{2}A_{1g}$ state (d_{z}^{2}) and $^{2}B_{1g}$ state ($d_{x}^{2}{}_{-y}^{2}$). Also, $^{2}T_{2g}$ state splits into $^{2}E_{g}$ state (d_{xz}, d_{yz}) and $^{2}B_{2g}$ (d_{xy}). Therefore, the three possible transitions are $^{2}B_{1g} \rightarrow {}^{2}A_{1g}$, $^{2}B_{1g} \rightarrow {}^{2}B_{2g}$, and $^{2}B_{1g} \rightarrow {}^{2}E_{g}$. According to the Jahn–Teller effect, a tetragonal elongation occurs along the Z-axis or a contraction in the equatorial XY- plane, which may ultimately result in a square planar environment. Figure 5 represents the ESR spectra of the Cu(II) complex. The results confirmed that the ground state is $^{2}A_{1g}$ because the value of $g_{\perp}$ (2.08841) is higher than that of $g_{\|}$ (2.03739). Hence, this indicates that the unpaired electron occupies d_z^2 orbital. The G parameter value was calculated according to Eq. (4).

$$G = \frac{g|| - ge}{g\perp - ge} = \frac{2.03739 - 2}{2.08841 - 2} = 0.4229 \tag{4}$$

The value of G is lower than 3 indicating a considerable interaction in the solid complexes [12, 14]. The magnetic moment of the Cu(II) complex is 1.80 BM., which is slightly higher than spin only value (1.73 BM). Hence, this clarifies the square planar environment of the Cu(II) complex.

3.2.3 FT-IR Spectra of Ag(I) and Cu(II) Schiff Base Complexes

The FT-IR spectra of Cu(II) and Ag(I) complexes are shown in Fig. 6A and B, respectively. The stretching vibration of the azomethine group was observed at 1600 and 1602 cm^{-1} for Ag(I) and Cu(II) complexes, respectively. Hence, the results revealed that the characteristic band of the azomethine group (–CH=N–) was shifted to a lower wavenumber compared to the free ligand. Hence, this indicating the formation of a coordination bond between the metal ion and the azomethine nitrogen. The broadband, which was appeared at 3448 and 3447 cm^{-1} for Ag(I) and Cu(II) complexes, are assigned to (–NH) stretching vibration, respectively. The disappearance of (–SH) stretching vibration in complexes, which was observed in ligand at 2747 cm^{-1}, confirms the (–NH) tautomer as shown in Scheme 1. The new bands, which were observed at 456, 486, 514, and 560 cm^{-1} in the case of Cu(II) complex, are assigned to (Cu–Cl), (Cu–S), (Cu–O), and (Cu–N) stretching vibrations, respectively. The new bands, which were observed at 419, 474, 535, and 566 cm^{-1} in the case of Ag(I) complex, are assigned to (Ag–Cl), (Ag–S), (Ag–O), and (Ag–N) bending vibrations, respectively [12, 14].

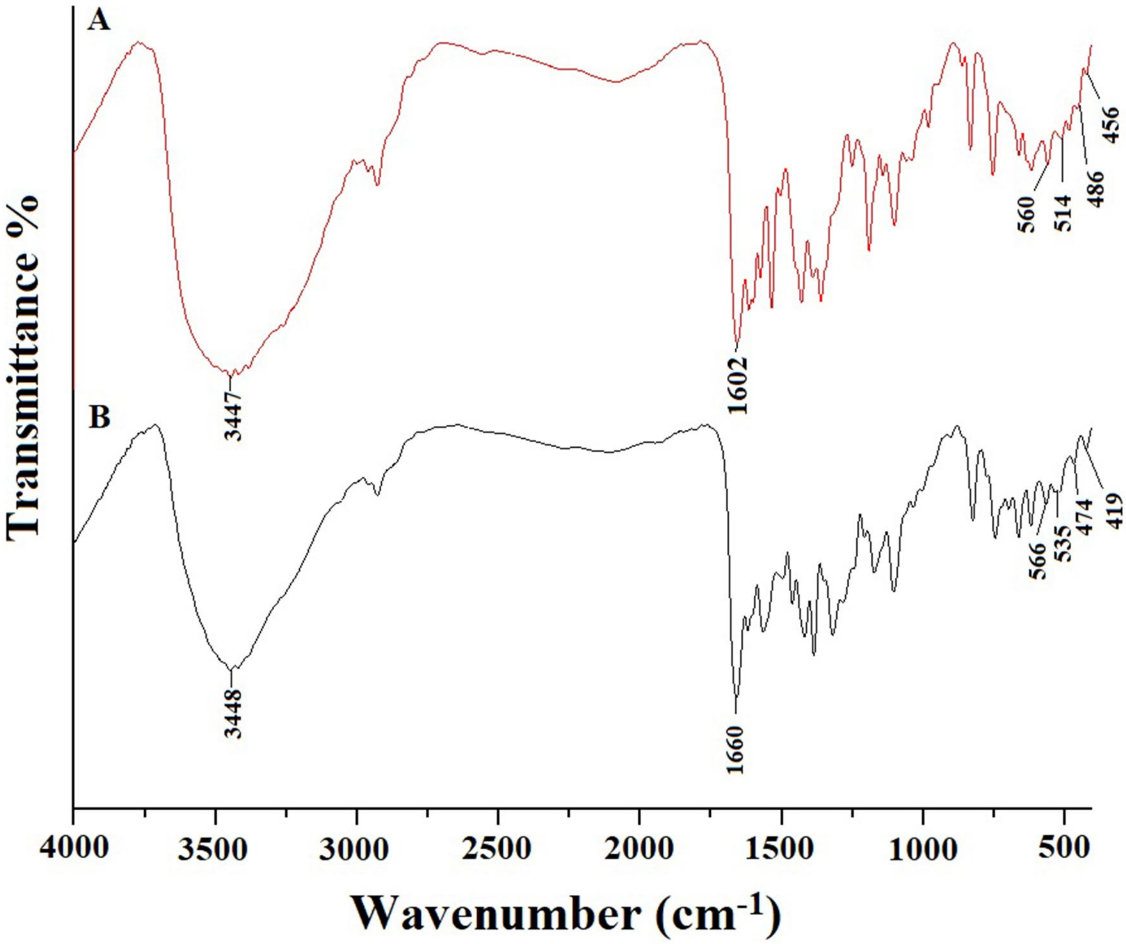

Fig. 6 FT-IR spectra of Cu(II) (**A**) and Ag(I) (**B**) complexes

Table 2 The electronic transitions of Cu(II) and Ag(I) complexes in Nujol mull

Compound	Wavenumber (cm^{-1}) Nujol mull	Assignment
Cu(II) complex	22,321	Charge transfer
	28,328	$^2B_{1g}\rightarrow{}^2A_{1g}$
	29,411	$^2B_{1g}\rightarrow{}^2E_g$
	31,250	$n–\pi^*$
	34,482	$\pi–\pi^*$
Ag(I) complex	24,630	Charge transfer
	30,211	$n–\pi^*$
	34,246	$\pi–\pi^*$

3.2.4 Electronic Spectra of the Complexes and Elemental Analysis

The electronic absorption data of Cu(II) and Ag(I) complexes in Nujol mull are listed in Table 2. The absorption bands of the Schiff base ligand ($\pi–\pi^*$, $n–\pi^*$, and charge transfer) are shifted to a higher wavelength (red-shift), confirming the coordination to the studied metal ions. Also, in the case of Cu(II) complex new bands appeared at 28,328 cm^{-1} with a shoulder at 29,411 cm^{-1} due to $^2B_{1g}\rightarrow{}^2A_{1g}$ and $^2B_{1g}\rightarrow{}^2E_g$ transitions, respectively [12–14]. The calculated percent of the elements of the Cu(II) complex ($C_{14}H_{13}ClCuN_4O_2S$) is 42.11%C, 3.28%H, 14.04%N, 8.02%O, 8.01%S, 8.77% Cl, 15.77% Cu. The practical percent of the elements of the Cu(II) complex is 42.34%C, 3.01%H, 14.23%N, 8.19%O, 7.86%S, 8.92% Cl, 15.45% Cu. The calculated percent of the elements of the Ag(I) complex ($C_{14}H_{15}Ag_2N_5O_6S$) is 28.24%C, 2.54%H, 11.77%N, 16.14%O, 5.37%S, 35.94% Ag. The practical percent of the elements of the Ag(I) complex is 28.33%C, 2.67%H, 11.86%N, 16.35%O, 5.27%S, 35.52% Ag. Hence, the results obtained from elemental analysis were in good agreement with theoretical values. Hence, this confirms the proposed formula of the synthesized complexes as shown in Scheme 2.

3.2.5 Thermal Analysis

Figure 7A and B represents thermogravimetric analysis (TGA) and differential scanning calorimetry (DSC) curves of Ag(I) and Cu(II) complexes, respectively. The Ag(I) complex showed a decomposition pattern with several steps. The first exothermic step which is located in the range from 54.41 to 243.19 °C, can be attributed to the loss of two coordinated water molecule with a weight loss of 6.09% (Calc. 6.06%). The second exothermic step which is located in the range from 243.19 to 302.31 °C, can be attributed to the loss of one HNO_3 molecule with a weight loss of 10.56% (Calc. 10.58%). The third exothermic step, which is located in the range from 302.31 to 1002 °C, can be assigned to the loss of ($CH_{10}N_4O$) with a weight loss of 15.41% (Calc. 15.82%) leaving ($2Ag + 13C + S$) with a percent of 67.94% (Calc. 67.54%).

Also, the Cu(II) complex is decomposed in a multi-steps. The first endothermic step, which is located in the range from 39.35 to 93.08 °C, can be attributed to the loss of one hydrated water molecule with a weight loss of 4.60% (Calc. 4.51%). The second exothermic step which is located in the range from 93.08 to 205.91 °C, can be attributed to the loss of one HCl molecule with a weight

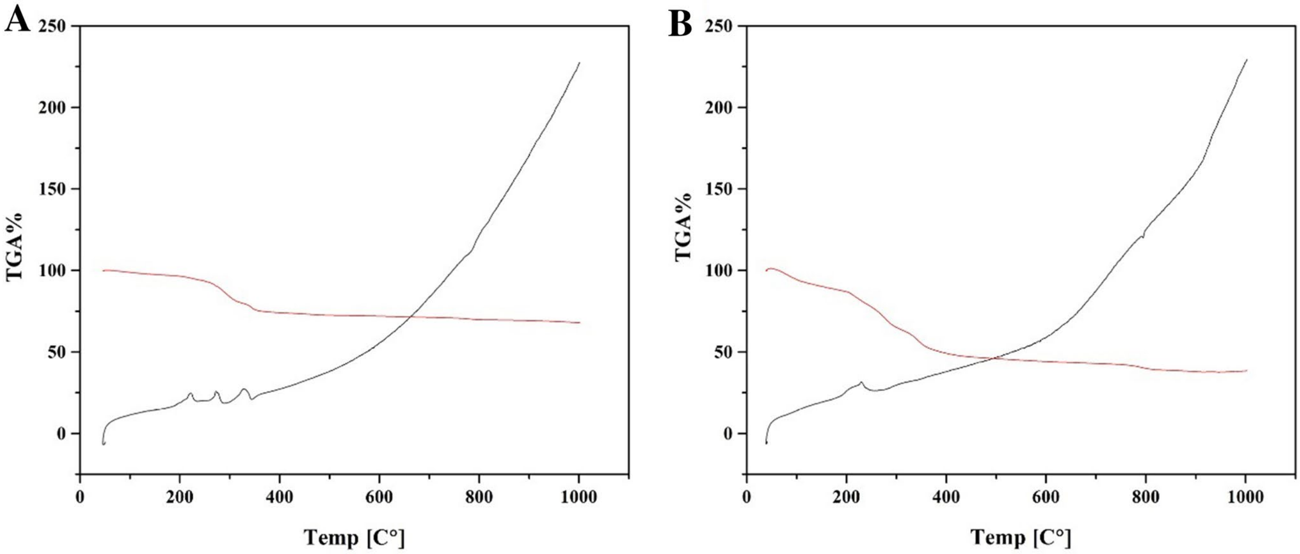

Fig. 7 TGA and DSC of Ag(I) (**A**) and Cu(II) (**B**) complexes

loss of 9.02% (Calc. 9.07%). The third exothermic step, which is located in the range from 205.91 to 950 °C, can be assigned to the loss of ($C_8H_{10}N_4S$) with a weight loss of 48.74% (Calc. 48.64%) leaving (CuO + 6C) with a percent of 37.64% (Calc. 37.78%).

3.3 Synthesis and Characterization of CuO and Ag Nanoparticles

The CuO and Ag nanoparticles were synthesized by thermal degradation of Cu(II) and Ag(I) complexes at 800 °C. The produced nanoparticles were characterized with various techniques.

3.3.1 X-ray Diffraction (XRD)

Figure 8A and B represents the XRD patterns of CuO and Ag nanoparticles, respectively. The results confirmed the presence of CuO (Monoclinic; ICDD No. 00-005-0661; and Space group: C2/c) with characterstic diffraction peaks at 2θ values = 35.43, 38.76, 48.66, 53.46, 58.38, 61.58, 65.87, 66.22, 68.05, 72.44 and 75.34° signifying (hkl) planes of $(\bar{1}\,11)$, (111), $(\bar{2}\,02)$, (020), (202), $(\bar{1}\,13)$, (022), $(\bar{3}\,11)$, (220), (311) and $(\bar{2}\,22)$, respectively [25–32]. The results confirmed the presence of Ag nanoparticles (Cubic; ICDD No. 00-003-0921; Space group: Fm$\bar{3}$m) with characteristic diffraction peaks at 2θ = 38.37, 44.57, 64.65, and 77.54° signifying (hkl) planes of (111), (200), (220), and (311), respectively [26–32]. Scherrer equation was used to determine the crystallite size (D) of the synthesized nanoparticles utilizing Eq. (5) [18].

$$D = \frac{0.9\lambda}{\beta cos\theta} \tag{5}$$

where λ, β, and θ are wavelength of Cu Kα X-ray (1.5406 Å), breadth of the diffraction peak at half maximum (radians), and Bragg's angle, respectively. The average crystallite size of CuO and Ag nanoparticles is 55.61 and 52.07 nm, respectively.

3.3.2 FT-IR

Figure 9A and B represents the FT-IR spectra of CuO and Ag nanoparticles, respectively. The characteristic bands, which were observed at 610 and 779 cm^{-1}, can be attributed to Cu–O stretching vibrations. The bands, which were observed at 3428 and 3426 cm^{-1}, are due to O–H stretching vibrations of the adsorbed water in CuO and Ag

Fig. 8 XRD patterns of CuO (**A**) and Ag (**B**) nanoparticles

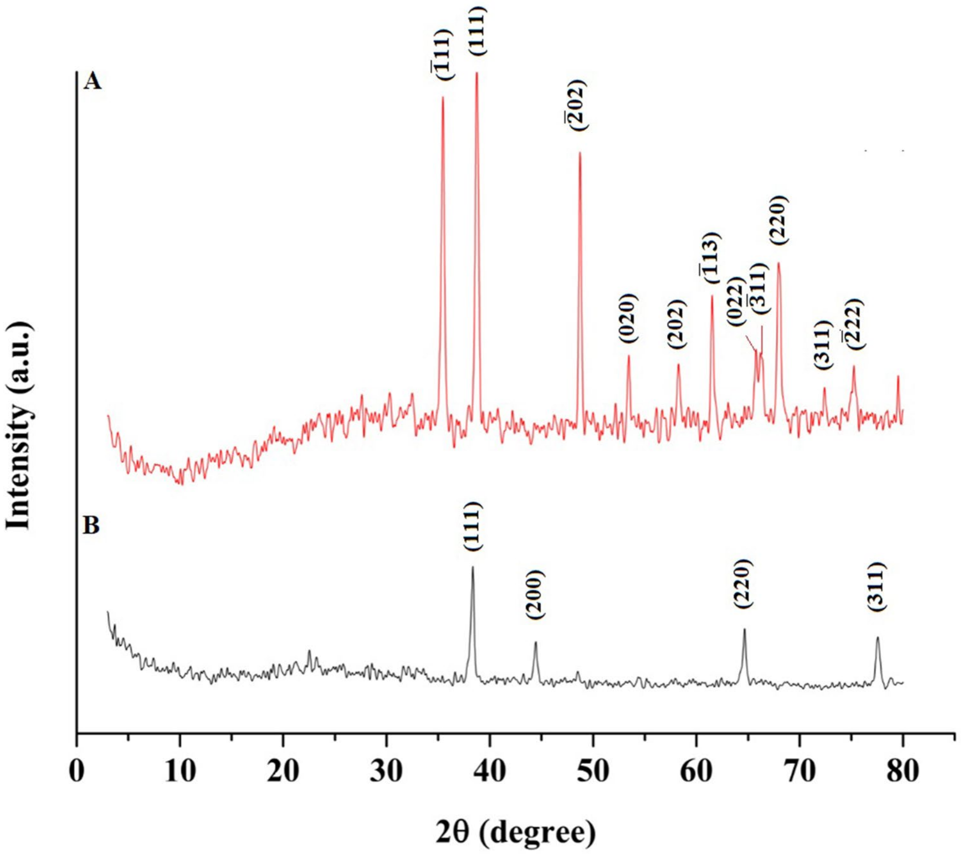

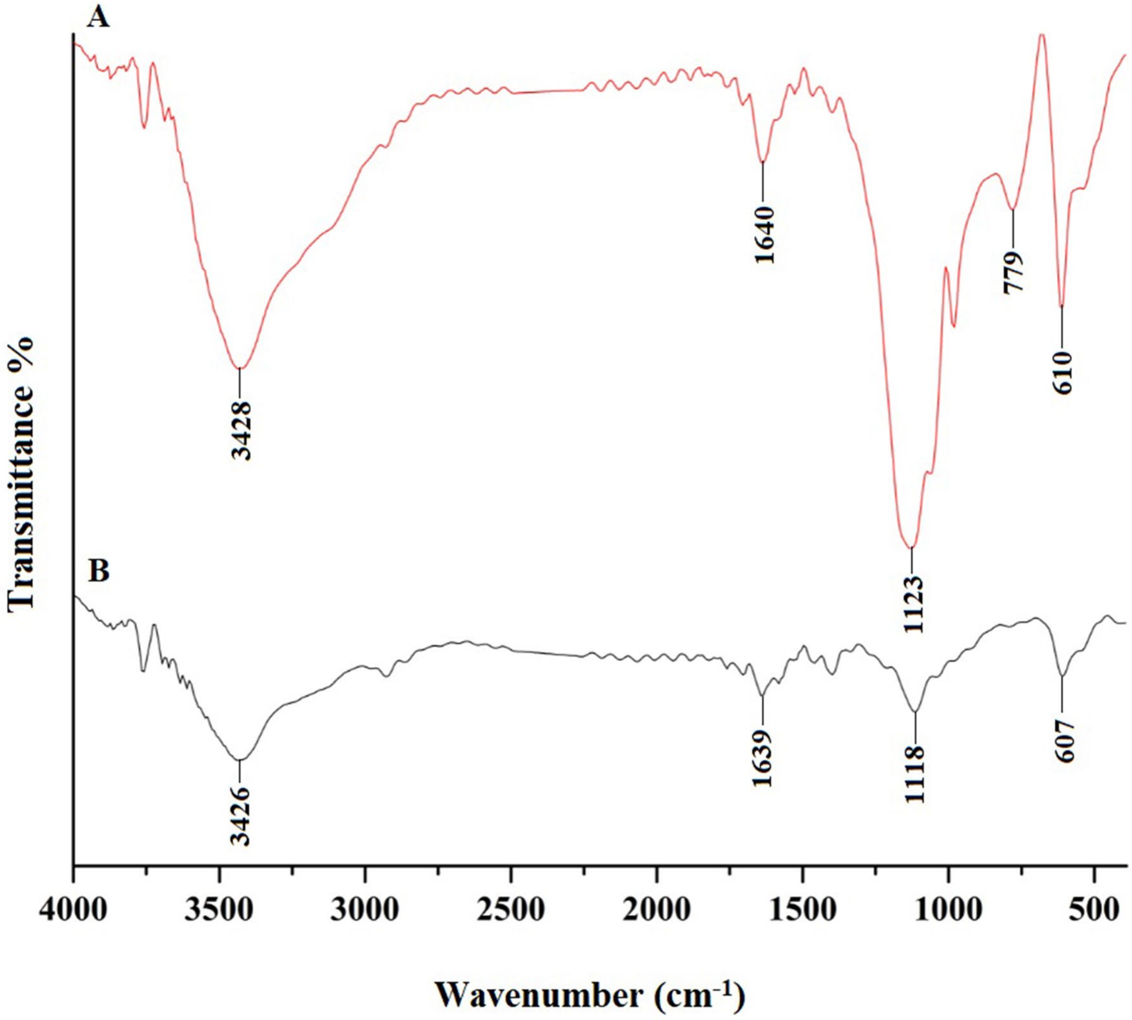

Fig. 9 FT-IR spectra of CuO (**A**) and Ag (**B**) nanoparticles

nanoparticles, respectively. Moreover, the bands, which were observed at 1640 and 1639 cm^{-1}, can be attributed to O–H bending vibrations of the adsorbed water in CuO and Ag nanoparticles, respectively [25, 26]. Besides, the observed other peaks are due to the residue of the organic parts.

3.3.3 FE-SEM and HR-TEM

Figure 10A and B represents the FE-SEM images of the CuO and Ag samples, respectively. The images show spherical and irregular shapes with an average grain size of 0.369 and 0.407 µm for CuO and Ag samples, respectively. Figure 11A and B represents the HR-TEM images of the CuO and Ag samples, respectively. The results show the presence of very tiny small spherical particles.

3.3.4 The Optical Band Gap

Figure 12A and B illustrates the optical band gap of CuO and Ag nanoparticles, respectively. The UV–Vis absorption data was obtained by measuring the absorbance versus wavelength for a suspension of CuO and Ag nanoparticles in Nujol mull. The optical band gap was calculated using Eq. (6) [18].

$$(\alpha h\nu)^{\frac{1}{n}} = K\left(h\nu - E_g\right) \tag{6}$$

where α, h, υ, n, K, and E_g are absorption coefficient, Planck constant, the frequency, integer represents the nature of transition (n = 0.5 for direct band gap and n = 2 for indirect band gap), proportionality constant, and the band gap energy, respectively. The optical band gap was determined by extrapolating a straight line at which $(\alpha h\upsilon)^2$ equals zero.

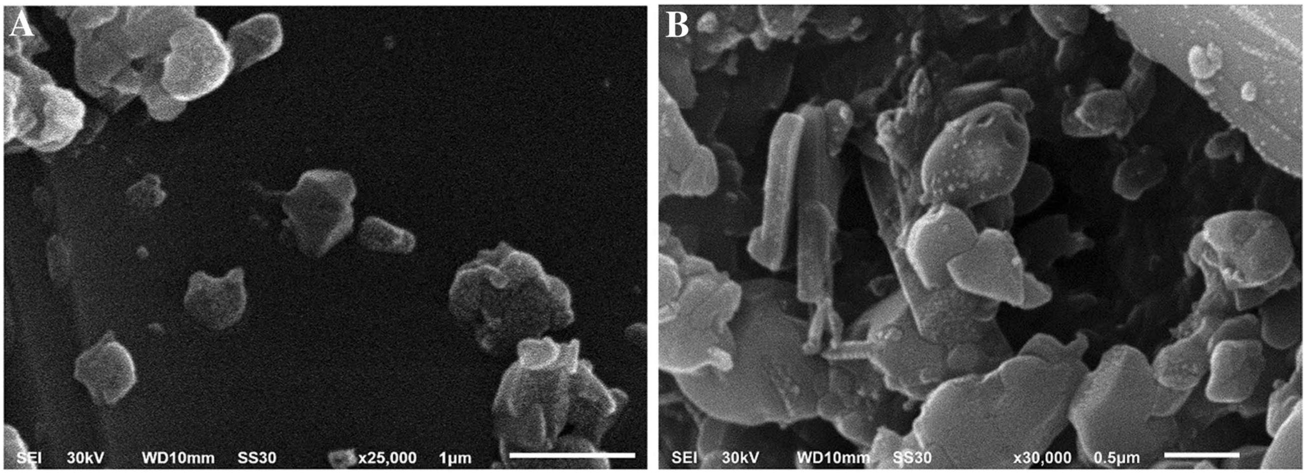

Fig. 10 FE-SEM images of CuO (**A**) and Ag (**B**) nanoparticles

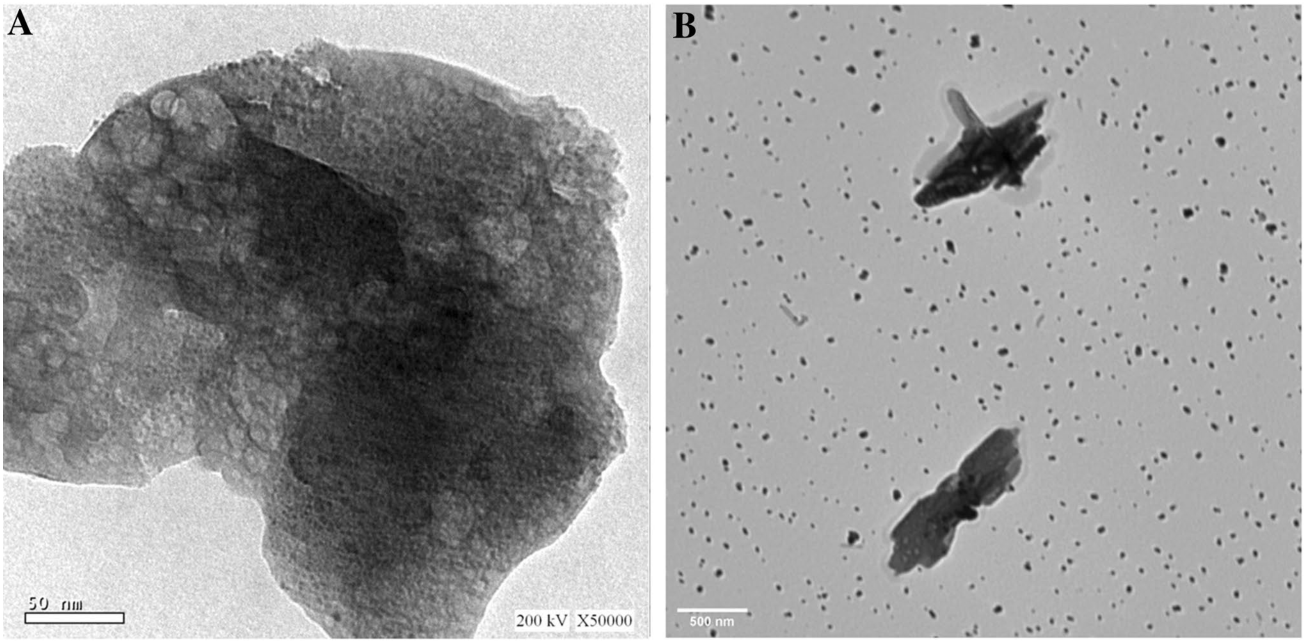

Fig. 11 HR-TEM images of CuO (**A**) and Ag (**B**) nanoparticles

The direct band gap of the CuO and Ag samples is 2.95 and 3.20 eV, respectively.

3.4 Photocatalytic Degradation of Methylene Blue Dye

The % degradation of methylene blue dye (MB) is 2.26% and 3.60 after 120 min in the case of utilizing (CuO + UV) and (Ag + UV), respectively. Figure 13A and B represents the relation between absorbance and wavelength at different times in the case of using ($CuO + H_2O_2 + UV$) and ($Ag + H_2O_2 + UV$), respectively. It was found that the absorbance values decreased with increasing time. Figure 14A and B represents the plot of % degradation (% D) versus time in the case of using ($CuO + H_2O_2 + UV$) and ($Ag + H_2O_2 + UV$), respectively. The results showed that the % degradation increased with increasing the time until equals 94.25% within 20 min and 90.42% within 210 min in case of utilizing ($CuO + H_2O_2 + UV$) and ($Ag + H_2O_2 + UV$), respectively. The kinetic performance of the photocatalytic degradation process was investigated using Eq. (7) [15].

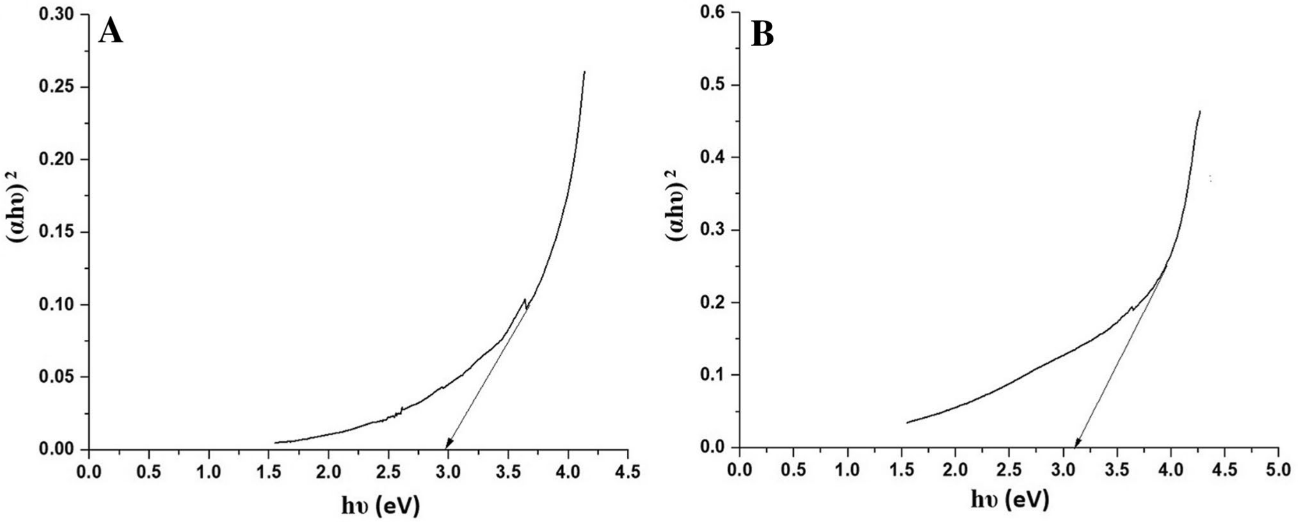

Fig. 12 The plot of $(\alpha h\upsilon)^2$ versus hυ curves of CuO (**A**) and Ag (**B**) nanoparticles

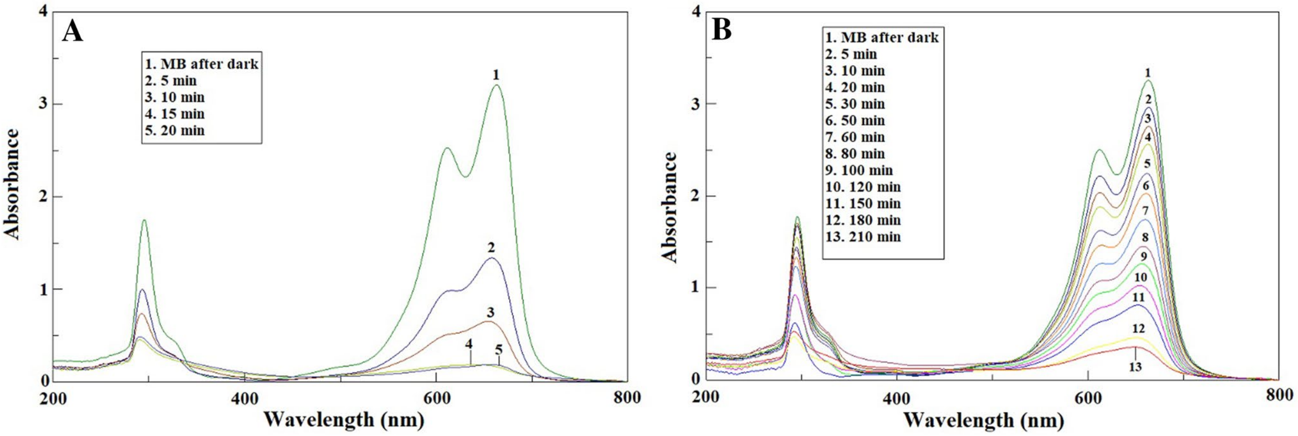

Fig. 13 The UV–Vis spectra of methylene blue dye in the case of using ($CuO + H_2O_2 + UV$) (**A**) and ($Ag + H_2O_2 + UV$) (**B**)

$$\ln\left(C_d/C_t\right) = \left(K_P\right) t \quad (7)$$

where K_P (1/min) is is the first-order rate constant. Figure 15A and B illustrates the relation between $\ln\frac{C_d}{C_t}$ and time in case of using ($CuO + H_2O_2 + UV$) and ($Ag + H_2O_2 + UV$), respectively. It was found that the photocatalytic degradation process follows the first-order. The rate constant (K_P) is 0.1502 and 0.01086 min^{-1} in case of using ($CuO + H_2O_2 + UV$) and ($Ag + H_2O_2 + UV$), respectively. The photocatalytic degradation of the MB dye using our prepared photocatalysts was compared with that of other photocatalysts in the literature. The results proved that our prepared photocatalysts possess high degradation efficiency as shown in Table 3 [14, 15, 27–32]. Scheme 3 illustrates the mechanism of the photocatalytic degradation of the methylene blue dye (MB) using the CuO and Ag samples. Upon the absorption of the incident UV light, an electronic transition takes place from the valence band to the conduction band. Thus, forming negatively charged electrons (e^-) at the conduction band leaving positively charged holes (h^+) at the valence band. Therefore, the holes react with the hydroxide anions to produce hydroxyl free radicals ($OH^\cdot$) whereas the electrons react with the dissolved oxygen to produce oxygen anion free radicals ($O_2^{-\cdot}$) which intern react with the hydrogen ion to produce superoxide free radicals ($HOO^\cdot$). After that, the superoxide free radicals were converted to hydroxyl free radicals. Finally, the hydroxyl free radicals work as an oxidizing agent and mineralize the methylene blue dye into non-toxic products such as CO_2 gas and water [15].

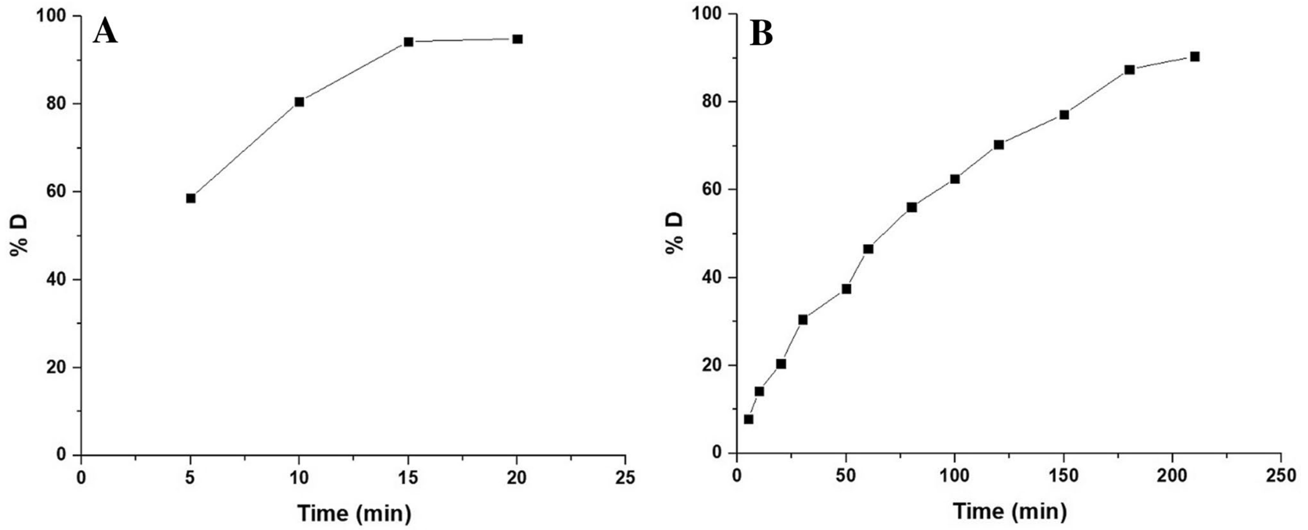

Fig. 14 The plot of % degradation versus time in the case of using (CuO + H_2O_2 + UV) (**A**) and (Ag + H_2O_2 + UV) (**B**)

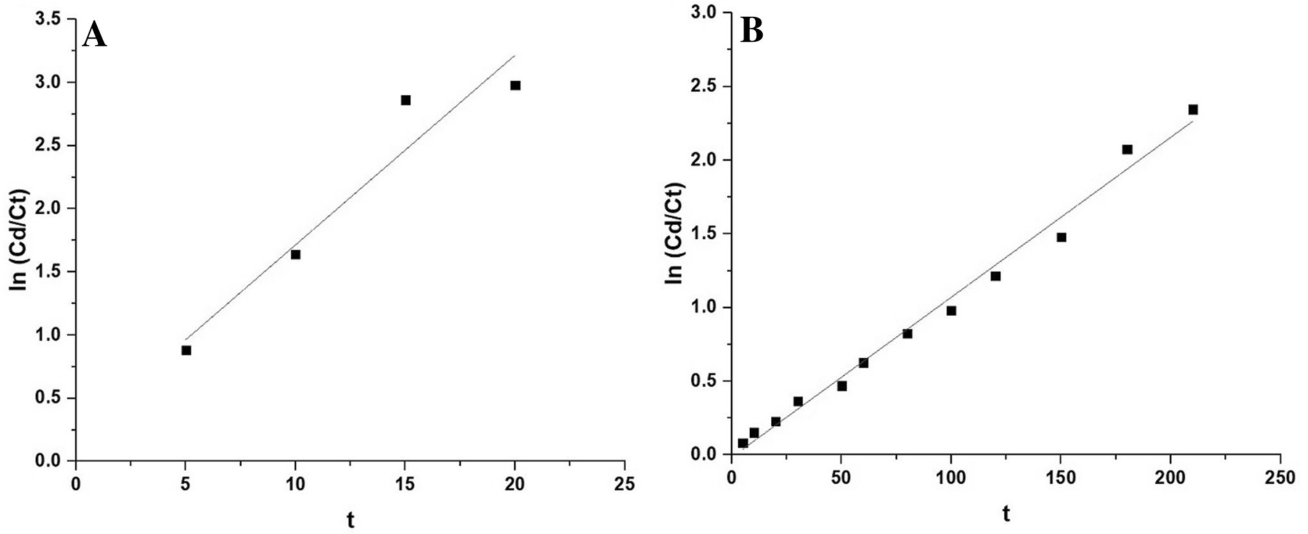

Fig. 15 The relation between $\ln\frac{C_d}{C_t}$ and time in the case of using (CuO + H_2O_2 + UV) (**A**) and (Ag + H_2O_2 + UV) (**B**)

Table 3 Comparasion between % degradation of methylene blue using comparison our prepared photocatalysts and other photocatalysts in the literature

Photocatalyst		Methylene blue dye		Irradiation source	% Degradation		References
Name	Weight (g)	Concentration (mg/L)	Volume (mL)		Value	Time (min)	
CuO	0.1	10	50	UV light	96.18	360	[14]
Fe_2O_3	0.1	20	50	UV light	100	40	[15]
CuO	0.1	20	50	UV light	94.25	20	This study
Co alloyed CdZnS	0.03	25	25	UV light	83	100	[27]
α-Fe_2O_3	0.1	10	100	Visible light	100	140	[28]
Ag	0.1	20	50	UV light	90.42	210	This study

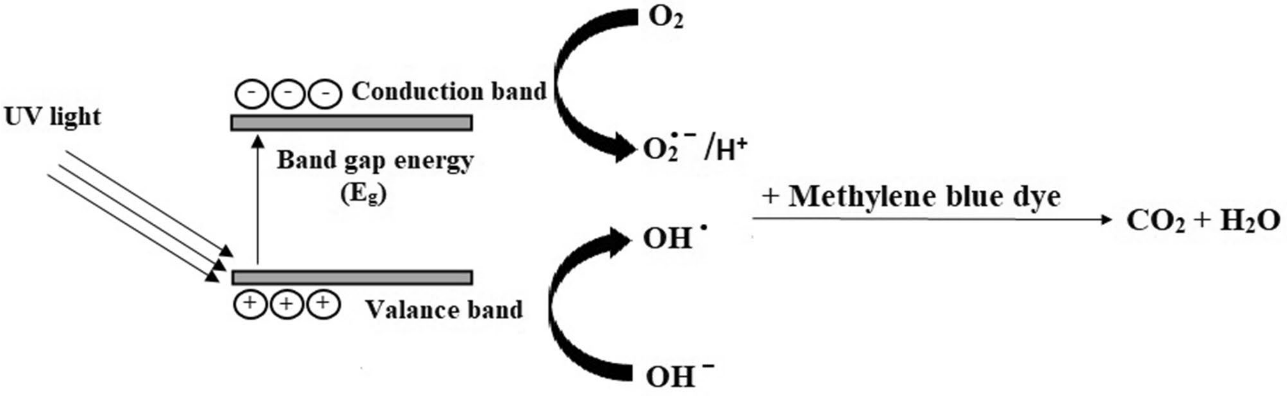

$$CuO/Ag + UV\ light \longrightarrow h^+\ at\ (VB) + e^-\ at\ (CB)$$

$$h^+ + OH^- \longrightarrow OH^\bullet$$

$$e^- + O_2 \longrightarrow O_2^{\bullet-}$$

$$O_2^{\bullet-} + H^+ \longrightarrow HOO^\bullet$$

$$2\ HOO^\bullet \longrightarrow H_2O_2 + O_2$$

$$H_2O_2 \xrightarrow{UV} OH^\bullet$$

Scheme 3 The photocatalytic degradation mechanism of the methylene blue dye (MB) using the CuO and Ag nanoparticles

Fig. 16 Inhibition zone diameters of the Schiff base ligand (**A**), Ag(I) complex (**B**), Cu(II) complex (**C**), Ag (**D**), and CuO (**E**) against *E. coli*

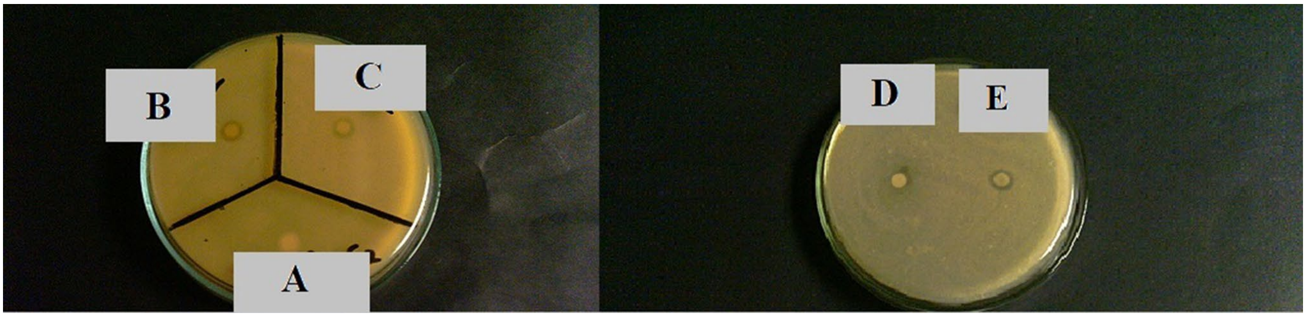

Fig. 17 Inhibition zone diameters of the Schiff base ligand (**A**), Ag(I) complex (**B**), Cu(II) complex (**C**), Ag (**D**), and CuO (**E**) against *S. aureus*

Table 4 The zone of inhibition of the synthesized compounds

Compound	Bacteria		Fungi	
	E. coli (G^-)	*S. aureus* (G^+)	*A. flavus*	*C. albicans*
Schiff base	0	0	0	0
Ag(I) complex	10	11	0	0
Cu(II) complex	11	11	0	0
CuO	12	12	0	0
Ag nanoparticles	9	10	0	0
Ampicillin standard	25	21	–	–
Amphotericin B	–	–	17	21

Table 5 The IC_{50} values of the synthesized compounds against MCF-7 cell line

Compound	Human breast cancer (MCF-7) IC_{50} (μg/mL)
Schiff base ligand	174 ± 3.7
Ag(I) complex	28.9 ± 1.2
Cu(II) complex	7.33 ± 0.6
CuO	48 ± 4.8
Ag	30.1 ± 2.1
Cisplatin standard	5.71

3.5 Biological Activity Studies

The Schiff base and their Ag(I) and Cu(II) complexes, as well as the nanoparticles (CuO and Ag) were tested for their antimicrobial activities against various microorganisms. They were evaluated as an antibacterial agent against *S. aureus* and *E. coli*. Also, they were evaluated as an antifungal agent against *A. flavus* and *C. albicans*. Figures 16 and 17 show the inhibition zone of the compounds against *E. coli* and *S. aureus*, respectively. The zone of inhibition for the synthesized compounds is presented in Table 4. It was concluded that the synthesized complexes and their nanoparticles show moderate activity against *E. coli* and *S. aureus* pathogens. Also, the synthesized Schiff base showed no activity against bacterial pathogens. Besides, all the products show no activity against fungal pathogens.

3.6 In Vitro Cytotoxic Activity

The synthesized compounds were screened for their cytotoxic activity against the MCF-7 cell line. Table 5 represents the IC_{50} values for the Schiff base, synthesized complexes (Ag(I) and Cu(II)), nanoparticles (CuO and Ag), and cisplatin as a standard drug. The results revealed significant inhibition of the compounds in the proliferation of

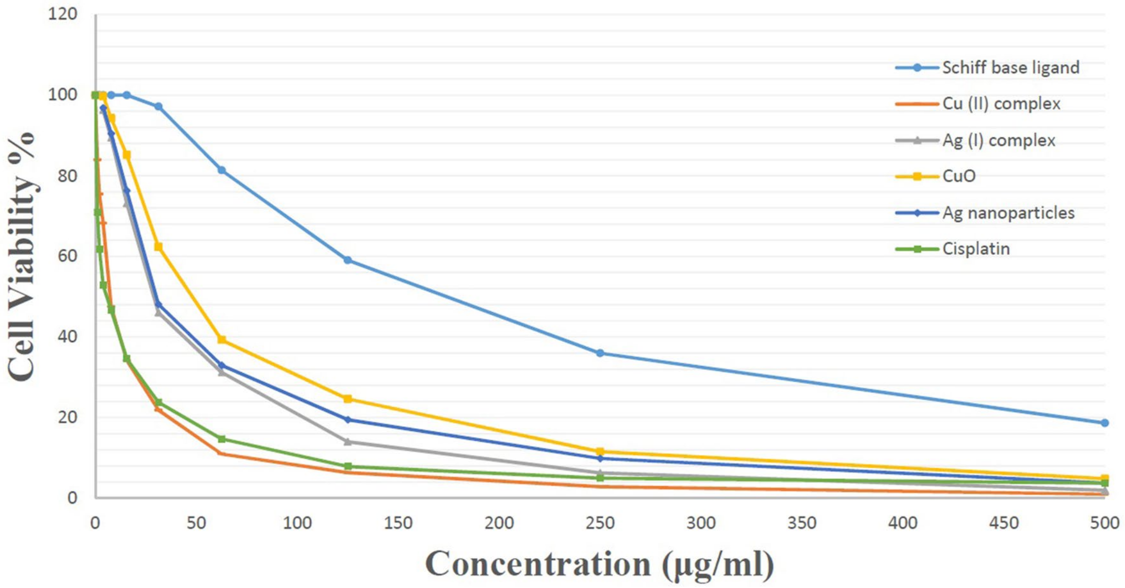

Fig. 18 In vitro cytotoxic activity of the samples against breast cancer cells (MCF-7)

breast cancer cells (MCF-7) in a dose-dependent manner as illustrated in Fig. 18. The Cu(II) complex can be nominated as a potential anticancer agent because it showed a cytotoxic activity ($IC_{50} = 7.33 \pm 0.6$ μg/mL) nearly equal to that of cisplatin drug ($IC_{50} = 5.71$ μg/mL). Also, Ag(I) complex, CuO, and Ag samples showed a moderate growth inhibition for the tested cancer cells whereas the Schiff base was the least active compound.

Declarations

Conflict of interest The authors declare that there is no conflict of interest for this paper.

References

1. D. Wu, L. Guo, S.-J. Li, Synthesis, structural characterization and anti-breast cancer activity evaluation of three new Schiff base metal (II) complexes and their nanoparticles. J. Mol. Struct. **1199**, 126938 (2020). https://doi.org/10.1016/j.molstruc.2019.126938
2. H. Keypour, M. Aidi, M. Mahmoudabadi, R. Karamian, M. Asadbegy, R.W. Gable, Synthesis, X-ray crystal structural, antioxidant and antibacterial studies of new Cu(II) macroacyclic Schiff base complex with a ligand containing homopiperazine moiety. J. Mol. Struct. **1198**, 126666 (2019). https://doi.org/10.1016/j.molstruc.2019.06.024
3. S. Jiang, H. Ni, F. Liu, S. Gu, P. Yu, Y. Gou, Binuclear Schiff base copper(II) complexes: syntheses, crystal structures, HSA interaction and anti-cancer properties. Inorg. Chim. Acta. **499**, 119186 (2020). https://doi.org/10.1016/j.ica.2019.119186
4. I. Bernadette Amali, M.P. Kesavan, V. Vijayakumar, N. Indra Gandhi, J. Rajesh, G. Rajagopal, Structural analysis, antimicrobial and cytotoxic studies on new metal(II) complexes containing N_2O_2 donor Schiff base ligand. J. Mol. Struct. **1183**, 342–350 (2019). https://doi.org/10.1016/j.molstruc.2019.02.005
5. A. Zianna, G.D. Geromichalos, A. Pekou, A.G. Hatzidimitriou, E. Coutouli-Argyropoulou, M. Lalia-Kantouri, A.A. Pantazaki, G. Psomas, A palladium(II) complex with the Schiff base 4-chloro-2-(N-ethyliminomethyl)-phenol: synthesis, structural characterization, and in vitro and in silico biological activity studies. J. Inorg. Biochem. **199**, 110792 (2019). https://doi.org/10.1016/j.jinorgbio.2019.110792
6. R. Kalarani, M. Sankarganesh, G.G.V. Kumar, M. Kalanithi, Synthesis, spectral, DFT calculation, sensor, antimicrobial and DNA binding studies of Co(II), Cu(II) and Zn(II) metal complexes with 2-amino benzimidazole Schiff base. J. Mol. Struct. **1206**, 127725 (2020). https://doi.org/10.1016/j.molstruc.2020.127725
7. C. Shiju, D. Arish, S. Kumaresan, Novel water soluble Schiff base metal complexes: synthesis, characterization, antimicrobial-, DNA cleavage, and anticancer activity. J. Mol. Struct. **1221**, 128770 (2020). https://doi.org/10.1016/j.molstruc.2020.128770
8. P.P. Utthra, N. Pravin, N. Raman, Scrutinizing the DNA damaging and antimicrobial abilities of triazole appended metal complexes. J. Photochem. Photobiol. B Biol. **158**, 136–144 (2016). https://doi.org/10.1016/j.jphotobiol.2016.02.033
9. M. Hanif, Z.H. Chohan, Synthesis, spectral characterization and biological studies of transition metal(II) complexes with triazole Schiff bases. Appl. Organomet. Chem. **27**, 36–44 (2013). https://doi.org/10.1002/aoc.2936
10. S. Amer, N. El-Wakiel, H. El-Ghamry, Synthesis, spectral, antitumor and antimicrobial studies on Cu(II) complexes of purine and triazole Schiff base derivatives. J. Mol. Struct. **1049**, 326–335 (2013). https://doi.org/10.1016/j.molstruc.2013.06.059
11. A.K. Singh, O.P. Pandey, S.K. Sengupta, Synthesis, spectral characterization and biological activity of zinc(II) complexes with 3-substituted phenyl-4-amino-5-hydrazino-1, 2, 4-triazole Schiff bases. Spectrochim. Acta Part A Mol. Biomol. Spectrosc. **85**, 1–6 (2012). https://doi.org/10.1016/j.saa.2011.08.019
12. M.Y. Nassar, H.M. Aly, M.E. Moustafa, E.A. Abdelrahman, Synthesis, characterization and biological activity of new 3-substitued-4-amino-5-hydrazino-1,2,4-triazole Schiff bases and their Cu(II) complexes: a new approach to CuO nanoparticles for photocatalytic degradation of methylene blue dye. J. Inorg. Organomet. Polym. Mater. **27**, 1220–1233 (2017). https://doi.org/10.1007/s10904-017-0569-x
13. M.Y. Nassar, H.M. Aly, E.A. Abdelrahman, M.E. Moustafa, Synthesis, characterization, and biological activity of some novel Schiff bases and their Co(II) and Ni(II) complexes: a new route for Co_3O_4 and NiO nanoparticles for photocatalytic degradation of methylene blue dye. J. Mol. Struct. **1143**, 462–471 (2017). https://doi.org/10.1016/j.molstruc.2017.04.118
14. H.M. Aly, M.E. Moustafa, M.Y. Nassar, E.A. Abdelrahman, Synthesis and characterization of novel Cu (II) complexes with 3-substituted-4-amino-5-mercapto-1,2,4-triazole Schiff bases: a new route to CuO nanoparticles. J. Mol. Struct. **1086**, 223–231 (2015). https://doi.org/10.1016/j.molstruc.2015.01.017
15. E.A. Abdelrahman, R.M. Hegazey, Y.H. Kotp, A. Alharbi, Facile synthesis of Fe_2O_3 nanoparticles from Egyptian insecticide cans for efficient photocatalytic degradation of methylene blue and crystal violet dyes. Spectrochim. Acta Part A Mol. Biomol. Spectrosc. **222**, 117195 (2019). https://doi.org/10.1016/j.saa.2019.117195
16. E.A. Abdelrahman, R.M. Hegazey, Exploitation of Egyptian insecticide cans in the fabrication of Si/Fe nanostructures and their chitosan polymer composites for the removal of Ni(II), Cu(II), and Zn(II) ions from aqueous solutions. Compos. Part B Eng. **166**, 382–400 (2019). https://doi.org/10.1016/j.compositesb.2019.02.027
17. R.M. Hegazey, E.A. Abdelrahman, Y.H. Kotp, A.M. Hameed, A. Subaihi, Facile fabrication of hematite nanoparticles from Egyptian insecticide cans for efficient photocatalytic degradation of rhodamine B dye. J. Mater. Res. Technol. **9**, 1652–1661 (2020). https://doi.org/10.1016/j.jmrt.2019.11.090
18. E.A. Abdelrahman, R.M. Hegazey, Facile synthesis of HgO nanoparticles using hydrothermal method for efficient photocatalytic degradation of crystal violet dye under UV and sunlight irradiation. J. Inorg. Organomet. Polym. Mater. **29**, 346–358 (2019). https://doi.org/10.1007/s10904-018-1005-6
19. A.M. Mansour, E.M. El Bakry, N.T. Abdel-Ghani, Photocatalytic degradation of methylene blue with copper(II) oxide synthesized by thermal decomposition of Flubendazole complexes. J. Photochem. Photobiol. A Chem. **327**, 21–24 (2016). https://doi.org/10.1016/j.jphotochem.2016.04.022
20. A. Muthuvel, M. Jothibas, C. Manoharan, Synthesis of copper oxide nanoparticles by chemical and biogenic methods: photocatalytic degradation and in vitro antioxidant activity. Nanotechnol. Environ. Eng. (2020). https://doi.org/10.1007/s41204-020-00078-w
21. A.W. Bauer, W.M.M. Kirby, J.C. Sherris, A.M. Turck, A. Von Graevenitz, 40 microbiology: a centenary perspective 1966 antibiotic susceptibility testing by a standardized single disk method. Am. J. Clin. Pathol. **45**(1978), 493–496 (1966)
22. M.A. Pfaller, L. Burmeister, M.S. Bartlett, M.G. Rinaldi, Multicenter evaluation of four methods of yeast inoculum

preparation. J. Clin. Microbiol. **26**, 1437–1441 (1988). https://doi.org/10.1128/jcm.26.8.1437-1441.1988

23. R.R. Aguilar, G.M. Fuentes, L.M. Aisa, V.G. Acosta, L.D. Martínez, L.A. Velasco, Uterine rupture in pregnant women with previous cesarean section after the Kristeller maneuver. Case report. Rev. Chil. Obstet. Ginecol. **79**, 111–114 (2014). https://doi.org/10.4067/s0717-75262014000200008
24. I. Mitra, S. Mukherjee, P.B. Reddy Venkata, S. Dasgupta, C.K. Jagadeesh Bose, S. Mukherjee, W. Linert, S.C. Moi, Benzimidazole based Pt(II) complexes with better normal cell viability than cisplatin: synthesis, substitution behavior, cytotoxicity, DNA binding and DFT study. RSC Adv. **6**, 76600–76613 (2016). https://doi.org/10.1039/c6ra17788c
25. K.S. Rathore, Deepika, N.S. Saxena, Study of structural and optical properties of ZnS: Cu nanoparticles. Adv. Sci. Lett. **22**, 3827–3830 (2016). https://doi.org/10.1166/asl.2016.8078
26. S.M. Hosseinpour-Mashkani, M. Ramezani, Silver and silver oxide nanoparticles: synthesis and characterization by thermal decomposition. Mater. Lett. **130**, 259–262 (2014). https://doi.org/10.1016/j.matlet.2014.05.133
27. S. Horoz, O. Baytar, O. Sahin, H. Kilicvuran, Photocatalytic degradation of methylene blue with Co alloyed CdZnS nanoparticles. J. Mater. Sci. Mater. Electron. **29**, 1004–1010 (2018). https://doi.org/10.1007/s10854-017-7999-7
28. A. Lassoued, M.S. Lassoued, B. Dkhil, S. Ammar, A. Gadri, RETRACTED ARTICLE: photocatalytic degradation of methylene blue dye by iron oxide (α-Fe_2O_3) nanoparticles under visible irradiation. J. Mater. Sci. Mater. Electron. **29**, 8142–8152 (2018). https://doi.org/10.1007/s10854-018-8819-4
29. M. Malathy, R. Jayasree, R. Rajavel, Facile synthesis of CuO nanoparticles from Cu(II) schiff base complexes: characterization, antibacterial and anticancer activity. Smart Sci. **5**, 100–115 (2017). https://doi.org/10.1080/23080477.2017.1328910
30. R. Al-Gaashani, S. Radiman, N. Tabet, A. Razak Daud, Synthesis and optical properties of CuO nanostructures obtained via a novel thermal decomposition method. J. Alloys Compd. **509**, 8761–8769 (2011). https://doi.org/10.1016/j.jallcom.2011.06.056
31. A. Ananth, S. Dharaneedharan, M.S. Heo, Y.S. Mok, Copper oxide nanomaterials: Synthesis, characterization and structure-specific antibacterial performance. Chem. Eng. J. **262**, 179–188 (2015). https://doi.org/10.1016/j.cej.2014.09.083
32. M. Zenasni, A. Quintero-Jaime, A. Benyoucef, A. Benghalem, Synthesis and characterization of polymer/V_2O_5 composites based on poly(2-aminodiphenylamine). Polym. Compos. **42**, 1064–1074 (2021). https://doi.org/10.1002/pc.25909